Multifunctional microcapsules: A theranostic agent for US/MR/PAT multi-modality imaging and synergistic chemo-photothermal osteosarcoma therapy

Hufei Wang [a,b,1], Sijia Xu [a,b,1], Daoyang Fan [c,1], Xiaowen Geng [d], Guang Zhi [d], Decheng Wu [a,b], Hong Shen [a,b], Fei Yang [a,b,*], Xiao Zhou [d,**], Xing Wang [a,b,***]

[a] Beijing National Laboratory for Molecular Sciences, Institute of Chemistry, Chinese Academy of Sciences, Beijing, 100190, China
[b] University of Chinese Academy of Sciences, Beijing, 100049, China
[c] Department of Orthopaedic, The First Affiliated Hospital of Zhengzhou University, Zhengzhou, 450000, China
[d] Department of Cardiology, Chinese PLA General Hospital, Beijing, 100853, China

ABSTRACT

Development of versatile theranostic agents that simultaneously integrate therapeutic and diagnostic features remains a clinical urgent. Herein, we aimed to prepare uniform PEGylated (lactic-co-glycolic acid) (PLGA) microcapsules (PB@(Fe_3O_4@PEG-PLGA) MCs) with superparamagnetic Fe_3O_4 nanoparticles embedded in the shell and Prussian blue (PB) NPs inbuilt in the cavity via a premix membrane emulsification (PME) method. On account of the eligible geometry and multiple load capacity, these MCs could be used as efficient multi-modality contrast agents to simultaneously enhance the contrasts of US, MR and PAT imaging. In-built PB NPs furnished the MCs with excellent photothermal conversion property and embedded Fe_3O_4 NPs endowed the magnetic location for fabrication of targeted drug delivery system. Notably, after further in-situ encapsulation of antitumor drug of DOX, (PB+DOX)@(Fe_3O_4@PEG-PLGA) MCs possessed more unique advantages on achieving near infrared (NIR)-responsive drug delivery and magnetic-guided chemo-photothermal synergistic osteosarcoma therapy. *In vitro* and *in vivo* studies revealed these biocompatible (PB+DOX)@(Fe_3O_4@PEG-PLGA) MCs could effectively target to the tumor tissue with superior therapeutic effect against the invasion of osteosarcoma and alleviation of osteolytic lesions, which will be developed as a smart platform integrating multi-modality imaging capabilities and synergistic effect with high therapy efficacy.

1. Introduction

Osteosarcoma is an aggressive malignant neoplasm that arises from primitive transformed cells of mesenchymal origin and triggers osteoblastic differentiation and malignant osteoid [1,2]. In general, therapeutic strategies comprise the aggressive multimodal therapy including preoperative (neoadjuvant) chemotherapy followed by surgical removal of all detectable disease, and postoperative (adjuvant) chemotherapy [3–5]. Currently, most active chemotherapeutic agents for osteosarcoma are a combination of high-dose methotrexate, doxorubicin, and cisplatin with the use of IFN-α or the recent immunomodulatory mifamurtide during adjuvant chemotherapy [6,7]. Despite their potent anticancer effect, chemotherapy treatments of osteosarcoma are associated with severely collateral toxic effects due to the lack of selectivity of these conventional anticancer drugs (cardiotoxicity, ototoxicity, nephrotoxicity, gonadal disfunction, midollar toxicity, etc.) [8], thereby causing serious damages to the normal tissue. In addition, personalized osteosarcoma treatment by chemotherapeutic drugs cannot be achieved, because it is extremely hard to trace the distribution of drugs in the tumor tissue, thus having no ability to provide timely feedback in clinic.

Scheme 1. Schematic illustration of US/MR/PAT multi-modality theranostic agents of (PB+DOX)@(Fe₃O₄@PEG-PLGA) MCs with NIR-responsive drug delivery and magnetic-guided chemo-photothermal synergistic therapy.

Particularly, on account of practical requirements for the removal of tumor tissues and simultaneous bone regeneration, contemporary clinical treatments of malignant bone tumors still encounter the significant challenges, and therefore pursuit of new platforms for desirable therapeutic outcomes is urgently needed.

Moderate hyperthermia (41–43 °C) is proved to be an effective way to inhibit tumor cell activity without obvious harm to normal tissues, and novel strategy has been developed to apply in cancer therapy [9,10]. Based on the little side effect and minimal invasive properties, photothermal therapy (PTT) is a safe and effective method for cancer treatment compared with the chemotherapy and radiotherapy, which can convert the light into heat energy under the irradiation of near-infrared (NIR, 700–1100 nm) laser and then increase temperature to the required level to efficiently kill tumor cells [11,12]. Such light window has been identified to exhibit intrinsic advantages of deeper tissue penetration and higher maximum permissible exposure as a respective result of reduced tissue scattering and lower energy of photons at longer wavelengths. On account of the heavy dependance on photothermal material for PTT efficiency, a suitable photothermal agent with an appropriate absorbance in NIR region, high photothermal conversion and low systemic toxicity is of great importance to the implementation of PTT. Although there are some kinds of developed photothermal therapeutic agents by PTT technique in cancer therapy, such as precious metal (gold nanorods, gold nanoplates, gold-silver alloy, etc.) [13–15], semiconductor nanomaterials (CuS, CuSe, MoS₂, etc.) [16–18], carbon nanomaterials (graphene, carbon nanoparticle, etc.) [19,20] and organic materials (polydopamine nanoparticle, polypyrrole nanoparticle, etc.) [21,22], the scattered light interference, nonuniform heat distribution of the edges and low energy penetration into the deep tissue make them insufficient effect to completely eradicate tumor tissue, resulting in the incomplete tumor ablation and tumor recurrence [23].

Compared to the single function of diagnosis or therapy, theranostic agents combine two functionalities into one "package", which is expected to overcome undesirable differences in biodistribution and selectivity of different diagnostic and therapeutic agents [24,25]. Therefore, combination of chemotherapy and photothermal therapy using nanomedicines is a highly effective strategy for osteosarcoma treatment. When photothermal treatment alone is insufficient to

completely ablate the tumor, the rising temperature can accelerate the drug release in the tumor to effectively kill the tumor [26,27]. Additionally, these chemo-photothermal agents are expectedly required to possess diagnostic function of ultrasound imaging (USI), photoacoustic tomography (PAT) imaging and magnetic resonance imaging (MRI) to achieve the high-resolution, high-contrast and multi-scale imaging from cells to tissues with a large depth [28,29] in tumor therapy, thus forming the integration of diagnosis and treatment. For example, Prussian blue (PB), as a typically photothermal agent approved by the Food and Drug Administration (FDA), possesses a strong metal-to-metal charge transfer absorption in the near-infrared region [30]. More importantly, PB shows a high absorbance in the NIR region (650–950 nm) and an excellent conversion capability, facilitating it as a new generation of NIR laser-driven photothermal agents for PTT. Therefore, PB nanoparticles (NPs) are explored as an excellent photo-absorbing agent for both PAT and PTT function for the oncotherapy [31,32]. Compared with Au NPs, PB NPs display the extremely low cost, high photostability, high molar extinction coefficient and clinically approved biosafety for human body [33]. Indocyanine green (ICG) is another FDA-approved agent for photothermal therapy [34], but its efficiency in photothermal therapy was limited because of the low photostability and insufficient tumor-homing ability [35,36]. Moreover, Fe₃O₄ NPs have attracted much attention because of its potential applications in magnetic separation, magnetic hyperthermia, magnetic targeting and magnetic resonance imaging. Among them, magnetically guided anti-cancer drug delivery system is a unique strategy to concentrate therapeutic nanoparticles to the tumor site to improve therapeutic effect [37,38]. Although T_2-weighted contrast agents are confused with other endogenous conditions that appear dark in MRI images, they have an obvious advantage due to the excellent strong contrast enhancement effects [39].

Therefore, a promising strategy on addressing undesirable difficulties is to apply theranostic nanomedicines with multi-modality imaging and synergistic chemo-photothermal osteosarcoma therapy, which simultaneously integrates the diagnostic and therapeutic agents into one single biological nanoplatform to significantly increase the accuracy of imaging diagnosis and boost the therapeutic effects. Here in this work, we proposed uniform PEGylated poly (lactic-co-glycolic acid) (PLGA) composite microcapsules of PB@(Fe₃O₄@PEG-PLGA) MCs with

superparamagnetic Fe_3O_4 NPs embedded in the shell and photothermal PB NPs encapsulated in the cavity via a premix membrane emulsification (PME) method [40–44]. PEG was selected as a hemocompatible and biocompatible chain to minimize toxicity to red blood cells and the body [45–47]. The incorporation of hydrophilic PEG segment within the hydrophobic PLGA developed the stealth MCs as a drug carrier system [48–52]. Their monodispersed core-shell structures and loading contrast agents empowered the MCs with excellent US/MR/PAT multi-modality imaging and photothermal conversion efficiency under 808 nm laser irradiation. Encouragingly, after further encapsulation of antitumor DOX within the cavity, $(PB+DOX)@(Fe_3O_4@PEG-PLGA)$ MCs could gather in the osteosarcoma under magnetic field, in which the local temperature rise by NIR irradiation thermally ablates osteosarcoma and detonates NIR-responsive DOX release, achieving a combined effect of photothermal therapy and chemotherapy for prominent anticancer efficacy (Scheme 1). This work paves a way for the rational design of theranostic platform for multimode imaging, magnetic targeting ability and NIR-triggered chemo-photothermal therapy for the diagnosis, localization, guidance, monitor and evaluation of tumor-related bone defects.

2. Materials and methods

2.1. Materials

Iron(III) acetylacetonate $(Fe(acac)_3)$, 1,2-hexadecanediol, oleylamine, polyethylene glycol (PEG), oleic acid, benzyl ether, cetyl trimethyl ammonium bromide (CTAB), $HAuCl_4$, $NaBH_4$, L-ascorbic acid, agar and doxorubicin (DOX) were purchased from J&K Scientific Ltd. Glycolide and Lactide were purchased from Purac (Netherlands) and further purified by recrystallization from ethyl acetate for several times. Stannous octoate, polyvinyl alcohol (PVA) and fluorescein diacetate were purchased from Sigma Aldrich. Fast membrane emulsification equipment (FMEM-500 M) and Shirasu porous glass (SPG) membrane were purchased from National Engineering Research Center for Biotechnology (Beijing). The glass membranes were annular cylinders (inner diameter = 8 mm, external diameter = 10 mm, length = 170 mm) with pore sizes of 7.2 μm. All other reagents were purchased from Beijing Chemical Reagents Company and used as received without further purification. Cells were supplied by China Infrastructure of Cell Line Resources.

2.2. Synthesis of Fe_3O_4 NPs

Oil-soluble Fe_3O_4 NPs were synthesized in terms of the previous literature [53]. Briefly, $Fe(acac)_3$ (1 mmol), 1,2-hexadecanediol (6 mmol), oleylamine (3 mmol), oleic acid (3 mmol) and benzyl ether (15 mL) were mixed together with magnetic stirring under a flow of argon, then the mixture was heated to 210 °C in an argon atmosphere. After maintaining at this temperature for 2 h, the mixture was heated to reflux (~310 °C) for 1 h with the color change from red-brown to black-brown. Next, it was cooled to room temperature via removal of the heat source. Following the post processing in the preparation of 4 nm of Fe_3O_4, black-brown n-hexane with 6 nm of Fe_3O_4 nanoparticles dispersed were obtained.

2.3. Synthesis of PB NPs

PB NCs were prepared according to the proceeding report [54]. Typically, 1 mmol citric acid was added into 40 mL of $FeCl_3$ aqueous solution (1.0 mM) under stirring at 60 °C. Then, 40 mL of $K_4[Fe(CN)_6]$ aqueous solution (1.0 mM) containing 1 mmol citric acid was added dropwise into the above solution under stirring at 60 °C. Immediately, a clear bright blue dispersion was formed during the mixing process, and allowed to be cooled down to room temperature with stirring continued for another 30 min. Afterwards, 80 mL of acetone was added into the

dispersion, and the mixture was centrifuged at 12000 rpm for 20 min to collect PB NCs, which were washed with acetone for three times. Finally, the obtained PB NCs were dissolved in water for future use.

2.4. Synthesis of gold nanorods

Gold nanorods (Au NRs) were prepared by seed-mediated growth method [55]. Briefly, seed solution was formed by adding ice-cold aqueous $NaBH_4$ (0.01 M) to a mixed aqueous solution of CTAB (0.10 M) and $HAuCl_4$ (0.01 M) under continuous stirring, then the solution was stirred for 2 min and kept at 25 °C for 2 h. Afterwards, the produced gold seed solution was added to a growth solution of CTAB (0.10 M), $AgNO_3$ (0.01 M), $HAuCl_4$ (0.01 M) and L-ascorbic acid (0.1 M) with gentle stirring. At last, the Au NRs were grown overnight without stirring at 30 °C.

2.5. Synthesis of PEG-b-PLGA

PEG-b-PLGA7030 was synthesized using PEG (Mw = 5000) as an initiatorvia the ring-opening polymerization of L-lactide and glycolide $(n_{LA}:n_{GA} = 70:30)$ [56,57]. Briefly, rigorously dried lactide (70 mmol), glycolide (30 mmol), PEG (0.14 mmol) and stannous octoate (0.05 wt% of lactide and glycolide) were transferred into a polymerization tube. After being purged with argon for three times, the tube was sealed in vacuum and heated to 170 °C for 20 h. In the next moment, the obtained product was dissolved in chloroform and then precipitated into ethanol, followed by being dried under vacuum at 35 °C to achieve a constant weight.

2.6. Preparation of MCs

$PB@(Fe_3O_4@PEG-PLGA)$ MCs were prepared via a two-step approach [41,42]. At the beginning, 300 mg of PEG-b-PLGA was dissolved in 10 mL dichloromethane, and a n-ethane dispersion of Fe_3O_4 NPs (0.5 mL, 2.5 wt%) was added under stirring. After the solvent was removed via reduced pressure distillation, the remained solid was redispersed by dichloromethane. Then, 4 mL of distilled water containing 8 mg of PB was mixed with 6 mL of the obtained dichloromethane containing 300 mg of PEG-b-PLGA and 8 mg of Fe_3O_4 under sonication to form an elementary emulsion. Secondly, the W/O emulsion was poured into aqueous external phase containing 1% w/w PVA with magnetic stirring for 120 s at 800 rpm to generate coarse double emulsion, which was then homogenized by squeezing them through the SPG membrane under a pressure of 90 kPa. Next, the yielded uniform double emulsion was transferred quickly into 600 mL of deionized water with magnetic stirring (500 rpm, 24 h) to solidify the $PB@(Fe_3O_4@PEG-PLGA)$ MCs, which were then collected via centrifugation (3000 rpm, 5 min) and washed by deionized water for three times, followed by being freeze-dried in a benchtop lyophilizer (ALPHA 1–2 LD, Christ). At last, the samples were stored in a fridge below 4 °C prior to performing experiments. $Au NR@(Fe_3O_4@PEG-PLGA)$ MCs were prepared in the same way.

$DOX@(Fe_3O_4@PEG-PLGA)$ MCs were similarly prepared by substituting Au NRs or DOX for PB. Briefly, 4 mL of distilled water containing 8 mg of DOX was mixed with 6 mL of dichloromethane containing 300 mg of PEG-PLGA and 8 mg of Fe_3O_4 under sonication to form an elementary emulsion. The W/O emulsion was poured into an aqueous external phase containing 1% w/w PVA under magnetic stirring to generate coarse double emulsion, which was then homogenized by squeezing them through the SPG membrane under a pressure of 90 kPa. Then the MCs were solidified by stirring, and centrifuged and lyophilized for use.

$(PB+DOX)@(Fe_3O_4@PEG-PLGA)$ MCs were prepared by dispersing 8 mg of PB and 8 mg of DOX in 4 mL of distilled water with continuous stirring. The remaining steps were the same as those stated above.

2.7. Characterization

Transmission electron microscopy (TEM) images of Fe_3O_4 NPs, PB NPs and Au NRs were captured on a JEOL 2100F electron microscopy with an acceleration voltage of 200 kV. X-ray diffraction (XRD) patterns of Fe_3O_4 and PB NPs were recorded by an X-ray diffractometer (XRD, D/max 2500, Rigaku). The absorbance spectra of PB NPs, Au NRs and MCs were measured by the UV–Vis spectra (TU901, Shimadzu). To determine the average molecular weight of the synthesized polymers, gel permeation chromatography (GPC, max VE-2001, Viscotek) measurement based on polystyrene standards was performed with chloroform as the eluent at a flow rate of 1.0 mL/min, and GPC results of the synthesized polymers were as follows: PLGA7030 ($M_w = 86500$, $M_w/M_n = 1.23$), PEG-b-PLGA7030 ($M_w = 87000$, $M_w/M_n = 1.22$).

The MCs were coated with gold palladium by sputter coater (E−1010; Hitachi) under vacuum and then observed by scanning electron microscopy (SEM, JSM-6700F, JEOL) with an accelerating voltage of 5 kV. The qualitative and quantitative chemical compositions analyses of the hybrid nano particles in the MCs were carried out by means of a multifunctional photoelectron spectrograph (XPS, ESCALAB250XI, VG). Fe_3O_4, PB inclusion mass fraction of MCs was determined by inductively coupled plasma mass spectrometry (ICP-MS, element, Finnigan), and the results were as follow: $Fe_3O_4 = {\sim}2.2$ wt%, PB $= {\sim}2$ wt%. The size distribution of MCs dispersed in distilled water were measured via dynamic light scattering method using a zetasizer (Nano ZS90, Malvern); While the magnetic properties of MCs were characterized by using a vibrating sample magnetometer (VSM, 7410, Lake Shore Cryotronics) at 37 °C. The MCs were analyzed with the simultaneous thermal analyzer (DSC, Q600, TA). The temperature ranged from 20 °C to 275 °C with the cooling rate of 10 °C/min.

2.8. In vitro US, MR and PAT imaging

In vitro USI was carried out under flow state to simulate the blood circulation. Firstly, a silicone tube (ID = 3 mm, OD = 6 mm) was set in a tank filled with degassed water with MCs evenly dispersed in. Then the dispersed solution flowed through the tube at a stable speed, and the process was captured by an ultrasonic imaging machine (Acuson Sequoia 512 system, Siemens) in B mode with 10 MHz ultrasound probe. All USI experiments were under the same parameters (Mechanical Index, MI = 0.49) and repeated for three times.

In vitro T_2-weighted MRI was acquired using a 7-T experimental MRI instrument (BioSpec 70/20 USR, Bruker). Even dispersions of MCs in normal saline with predetermined concentrations were placed in a series of tubes for T_2-weighted MRI, and after careful preparation, the tubes were scanned in a 7-T MRI system.

In vitro PAT was performed with a photoacoustic tomography system (MOST invision 128, iThera). Homogeneous dispersions of MCs in normal saline with desired concentrations were transferred to the containers made of agar, and after being sealed, the containers were scanned in the photoacoustic tomography system.

2.9. The encapsulation efficiency (EE) of DOX

Fe_3O_4 NPs were removed via an external magnetic field after dissolving the (PB+DOX)@(Fe_3O_4@PEG-PLGA) MCs in chloroform, then quantitative water was used to extract the DOX. The DOX content in (PB+DOX)@(Fe_3O_4@PEG-PLGA) MCs was calculated via the UV–vis spectra measurement (TU901, Shimadzu). All of the experiments were repeated in triplicate for precision. EE was calculated as follows:

$$EE(\%) = (\text{the amount of loaded drug})/(\text{the amount of drug initially})$$
$$\times\, 100\%$$

2.10. In vitro drug release

DOX release from the (PB+DOX)@(Fe_3O_4@PEG-PLGA) MCs was measured using saline as the release medium. Briefly, four groups of (PB+DOX)@(Fe_3O_4@PEG-PLGA) MCs (3 mg) were respectively transferred into pre-swollen dialysis bags (MWCO: 3500 Da), which were then placed in wild-mouth bottle filled with 100 mL of saline with shaking at 100 rpm at 37 °C. Three bottles containing (PB+DOX)@(Fe_3O_4@PEG-PLGA) MCs were exposed to magnetic field for 20 min. Then, three other bottles containing (PB+DOX)@(Fe_3O_4@PEG-PLGA) MCs were exposed to 808-nm NIR laser at output power of 0.8 W for 20 min. Simultaneous application of 808-nm NIR laser and magnetic field in the last set of bottles for 20 min. Besides, the release medium was withdrawn and replenished with a fresh medium at every predetermined interval. Finally, the concentration of DOX in the release medium was determined by the UV–vis spectra measurement.

2.11. In vitro cell toxicity

Mouse embryonic fibroblasts (NIH/3T3) were adopted to evaluate *in vitro* cell toxicities of the MCs. First of all, the cells were cultured in α-MEM supplemented with 10% fetal bovine serum in an atmosphere of 5% CO_2 at 37 °C. After being sterilized by 70% ethanol solution for 40 min, different MCs with desired concentration (5 mg/mL) were transferred into wells of 96-well culture plate, respectively. Then, 80 μL of cell suspension with 1×10^5 cells were seeded into each well. After cell-seeded MCs were maintained under 5% CO_2 at 37 °C for 3 h, and 240 μL of culture medium was added to each well. The viability and proliferation of NIH/3T3 cells cultured together with microcapsules for 1, 3 and 6 days were determined by CCK-8 assay. At each predetermined interval, original culture medium in each well was removed following by addition of fresh culture medium (100 μL). After adding CCK-8 solution (10 μL) into each well, NIH/3T3 cells were incubated at 37 °C under 5% CO_2 for 4 h, and the absorbance of culture medium was measured at 450 nm using micro-plate reader (Sunrise, Tecan, Austria).

2.12. In vivo US, MR and PAT imaging

In vivo USI was carried out on young New Zealand rabbits (provided by animal center of Chinese PLA General Hospital; male or female; 16–20 g of body weight), which were anesthetized with chloral hydrate (10 wt%) first off, and then their hearts were imaged by an ultrasonic imaging machine (Acuson Sequoia 512 system, Siemens) in B mode with 10 MHz ultrasound probe before and after injection with 2 mL of normal saline containing 4.8 mg of PB@(Fe_3O_4@PEG-PLGA) MCs via ear vein using a syringe.

In vivo MRI was performed on osteosarcoma-bearing nude mice by a 7-T experimental MRI instrument (BioSpec 70/20 USR, Bruker). The nude mice were firstly anesthetized with isoflurane, and T_2-weighted images of them were taken before and after injecting 250 μL of normal saline containing 0.6 mg of PB@(Fe_3O_4@PEG-PLGA) via tail vein. And then, an external magnetic field was applied on the tumor for 20 min, followed by T_2-weighted MRI, and the imaging parameters were set as follows: repetition time (TR) = 3000 ms; echo time (TE) = 40.6 ms; field of view (FOV) = 50 mm × 50 mm; slice thickness = 1 mm.

In vivo PAT was done on 6-week-old nude mice using a photoacoustic tomography system (MOST invision 128, iThera) at the scan wavelength of 808 nm, and PAT images of the mice were acquired before and after injection of 250 μL of normal saline containing 0.6 mg of PB@(Fe_3O_4@PEG-PLGA) MCs via tail vein.

2.13. Photothermal effect of MCs

Homogeneous dispersions of (PB+DOX)@(Fe_3O_4@PEG-PLGA) MCs and DOX@(Fe_3O_4@PEG-PLGA) MCs (5 mg/mL) were prepared in saline and then put into thermostatic water bath at 37 °C with the irradiation
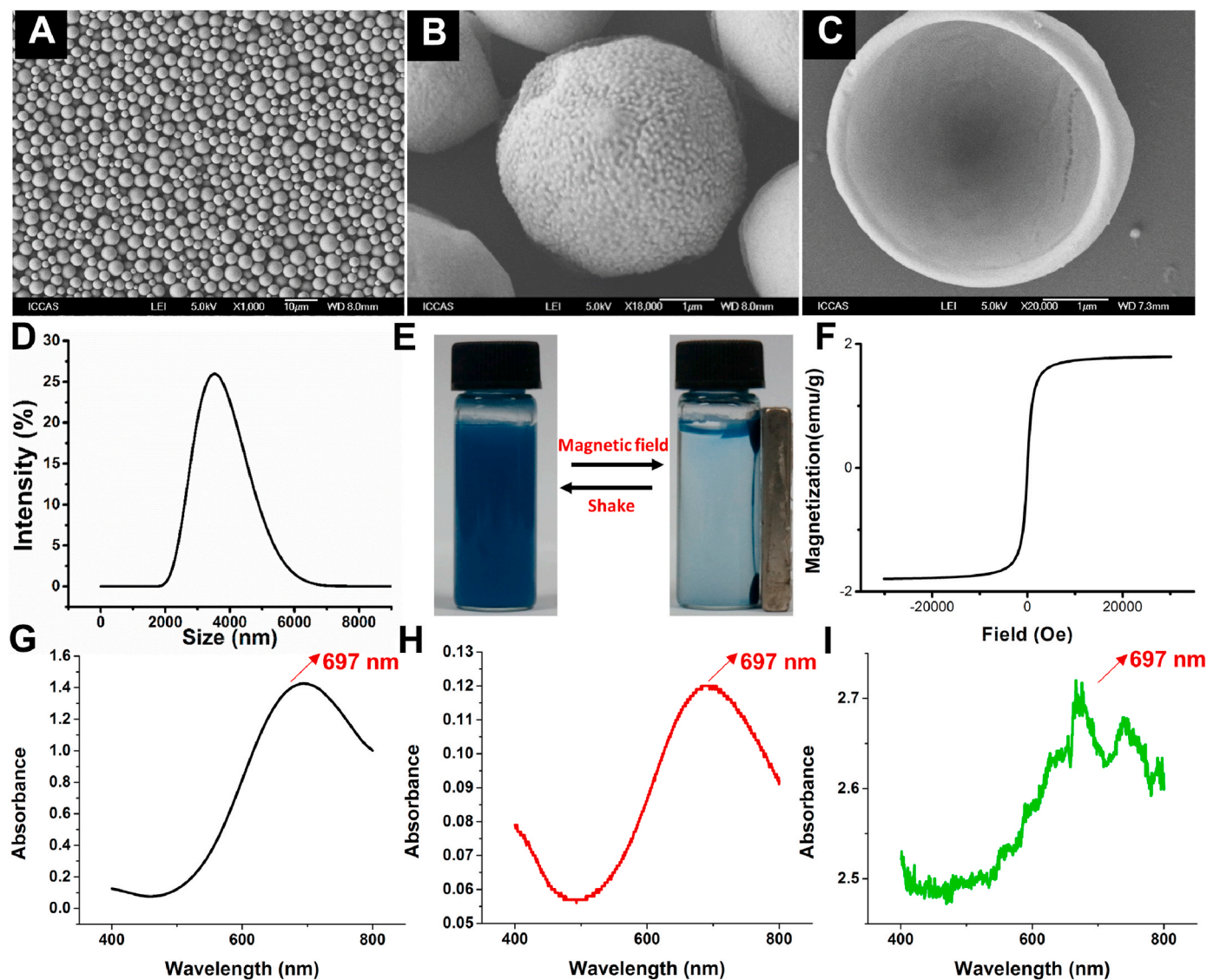
Fig. 1. Characterization of PB@(Fe$_3$O$_4$@PEG-PLGA) MCs. SEM images of MCs with (A) Low and (B) High magnification; (C) SEM image of one MC cut by a super thin blade; (D) Size distribution; (E) Magnetic property upon exposure to an external magnet; (F) Hysteresis loops. UV–vis spectra of (G) PB NPs in water, (H) PB NPs in water extracted from PB@(Fe$_3$O$_4$@PEG-PLGA) MCs and (I) PB@(Fe$_3$O$_4$@PEG-PLGA) MCs in water.

by 808-nm NIR laser (Hi-Tech Optoelectronics Co., Ltd.) at output power of 0.8 W/cm^2. After 27 min of irradiation, the laser was turn off for 18 min, and the operation was repeated for three times. The temperature variations of the dispersions were monitored by a digital thermometer every second, while the heating curve was determined by plotting the temperature.

2.14. In vitro photothermal therapy

To further study the effect of photothermal therapy, tumor cells were treated with (PB+DOX)@(Fe$_3$O$_4$@PEG-PLGA) MCs in different conditions. Cells were cultured as described above and then incubated with (PB+DOX)@(Fe$_3$O$_4$@PEG-PLGA) MCs for 4 h, followed by exposing under NIR laser (0.8 W/cm^2) or/and magnetic field for 10 min. Then the cells were incubated at 37 °C for 12 h and measured by CCK-8 assay. In addition, calcein AM/Propidium Iodide (PI) Detection Kit was introduced to further study cell survival efficiency. 143B cells were seeded in 12-well plate (5 × 10^4 cells/well) until attachment. Then the (PB+DOX)@(Fe$_3$O$_4$@PEG-PLGA) MCs were added. Each group of cells was processed as described above. Then, cells were stained with Calcein AM/PI detection kit according to the instructions. A fluorescence microscope

(Axio Observer, Carl Zeiss) was introduced to capture fluorescence images.

2.15. In vivo photothermal therapy

36 healthy female Balb/c nude mice (about 4 weeks old) were used to build tumor models. 1 × 10^7 143B cells in 100 μL of saline were injected into the joint cavity of the right hind leg of each mouse. The nude mice were separated into 6 groups (n = 6 per group), and 100 μL of saline, DOX, (PB+DOX)@(Fe$_3$O$_4$@PEG-PLGA) (5 mg/mL) and PB@(Fe$_3$O$_4$@PEG-PLGA) (5 mg/mL) were injected via the tail vein. Two groups were selected as irradiation groups. An external magnetic field was applied on the tumor site for 20 min, and then the tumor sites were irradiated with the 808-nm laser (0.8 W/cm^2), with each mouse irradiated for 10 min every 48 h. Infrared thermographic images and temperature of the tumors were monitored by an infrared thermal imaging camera (FLIRA615, Pumeng Technology Co., LTD, Shanghai) simultaneously. The tumor sizes were measured using a caliper at the widest point and the perpendicular length. The tumor volumes were calculated based on the following formula: volume (V) = (tumor length) × (tumor width)^2/2. The tumor volume was regarded as "0" at its disappearance.
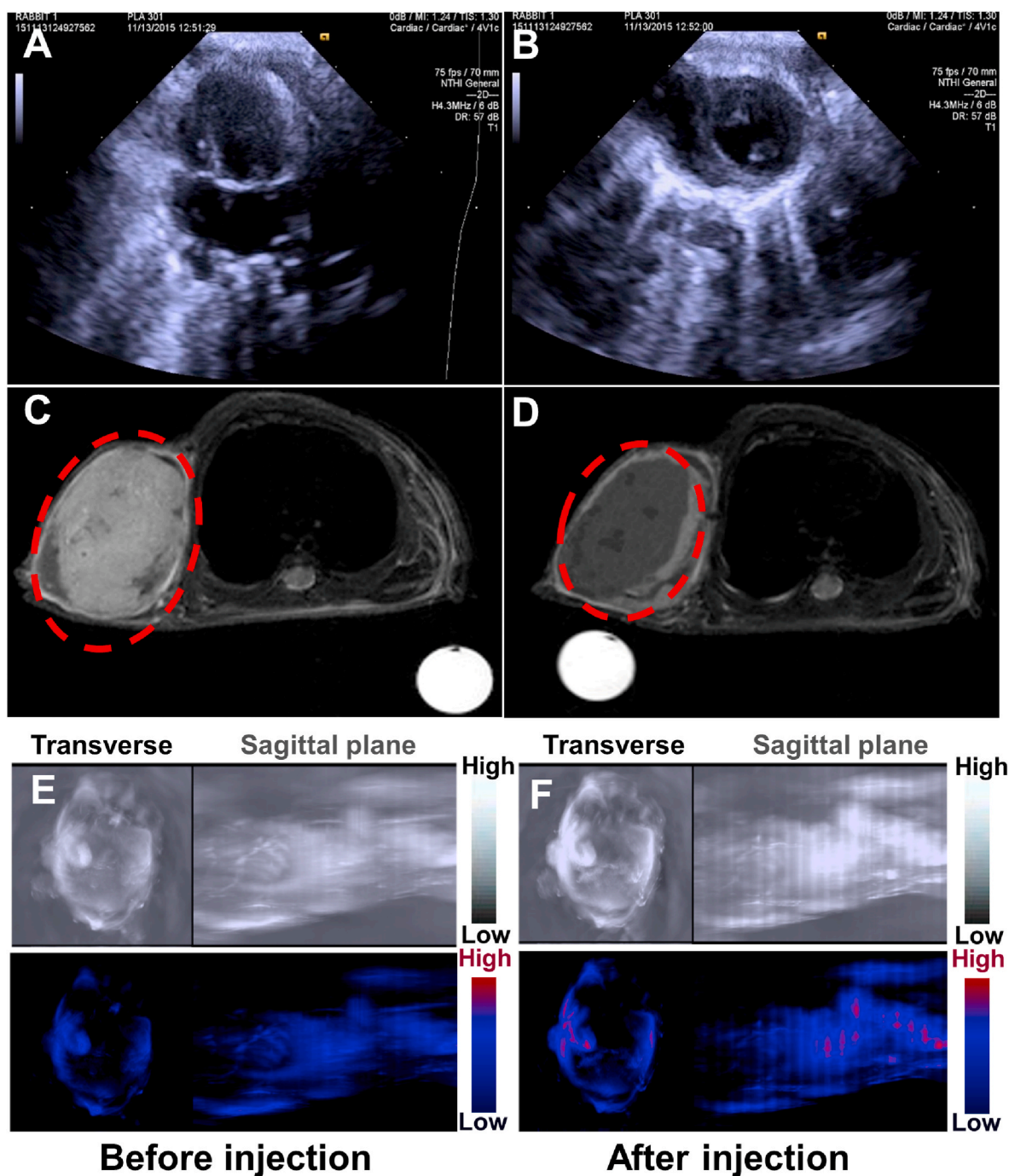
Fig. 2. *In vivo* US/MR/PAT imaging. *In vivo* USI of the heart in the rabbit before (A) and after (B) injection of PB@(Fe$_3$O$_4$@PEG-PLGA) MCs. *In vivo* T_2-weighted images of osteosarcoma in nude mice before (C) and after (D) injection of PB@(Fe$_3$O$_4$@PEG-PLGA) MCs. *In vivo* PAT images of nude mice before (E) and after (F) being injected with PB@(Fe$_3$O$_4$@PEG-PLGA) MCs. Top row: grey image; bottom row: color-coded image. Left: transverse plane; right: sagittal plane.

2.16. Micro-CT analysis

After removing the right hind legs of nude mice, high-resolution micro-CT was performed with an Inveon MM system (Siemens, Munich, Germany) to measure bone growth in each specimen. Each specimen was analyzed with segmentation software, and the analyzed region of interest included the bone at osteosarcoma plus the bone proximal to it, whose boundary was manually positioned for definition. The experiment was blinded to all groups being assessed. Three-dimensional reconstructions were made with two-dimensional images using a 3D visualization system (Inveon Research Workplace, Siemens, Munich, Germany). Bone mineral density (BMD) and bone growth were

obtained.

2.17. Histological analysis

On day 28, the nude mice were sacrificed and autopsied to collect the main organs (heart, liver, spleen, lung and kidney) and the tumor tissues. Finally, the main organs and tumor issues were stained with hematoxylin and eosin (H&E) for the detection of changes in the cellular integrity and tissue morphology. The tumor slices were also stained with Masson's trichrome stains and terminal deoxynucleotidyl transferase biotin-dUTP nick-end labeling (TUNEL assay) to detect apoptotic or necrotic cells. Finally, the images of the stained tumor and organ slices
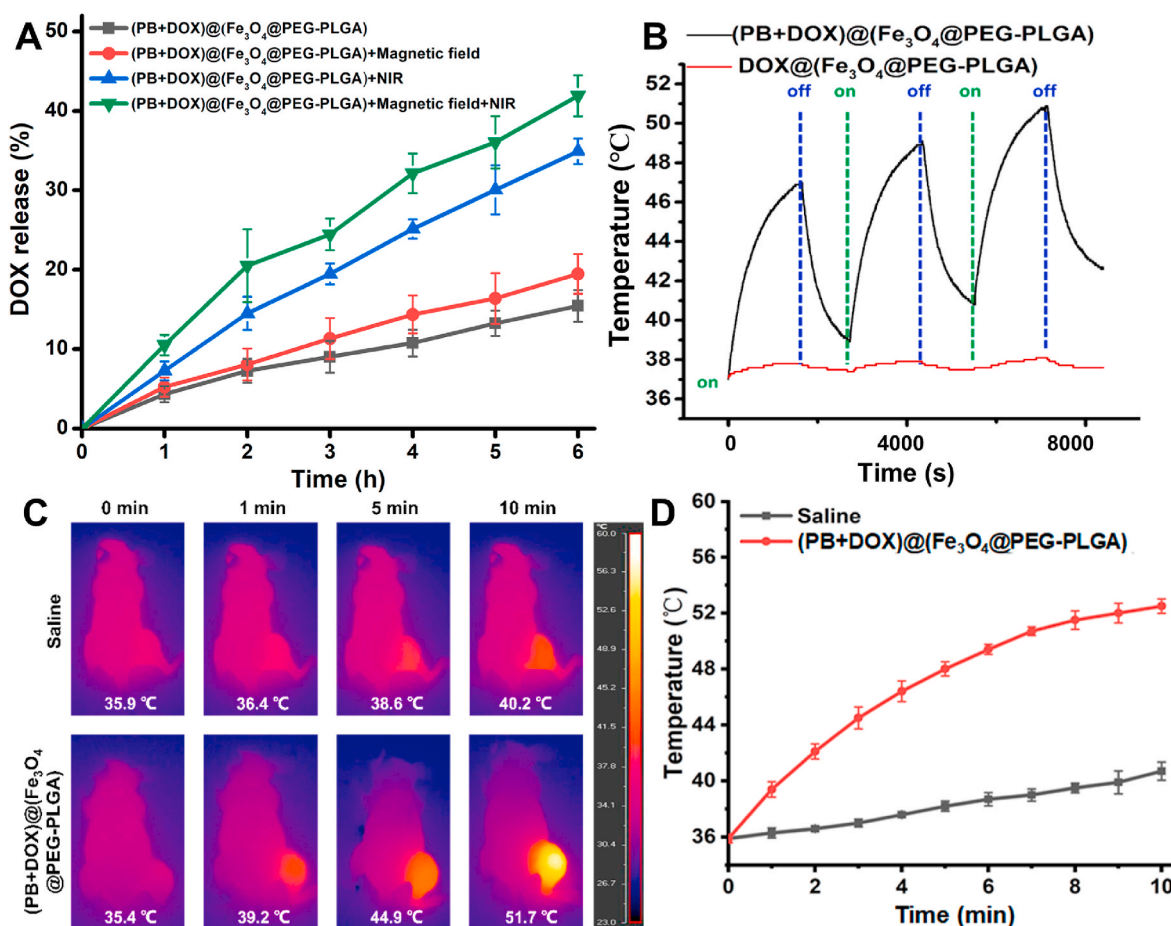
Fig. 3. NIR-responsive drug delivery and photothermal therapy. (A) Temperature variations of DOX@(Fe$_3$O$_4$@PEG-PLGA) and (PB+DOX)@(Fe$_3$O$_4$@PEG-PLGA) MCs with irradiation of 808-nm NIR laser. On: turn on the laser; off: turn off the laser. (B) DOX release from (PB+DOX)@(Fe$_3$O$_4$@PEG-PLGA) MCs with and without magnetic field and irradiation of 808-nm NIR laser. (C) Infrared thermographic maps. The temperature shown in the figure represents the highest temperature and the color bar represents the relative temperature. (D) Time-dependent temperature increase in the tumor-bearing nude mice irradiated by the 808-nm NIR laser after tail vein injection with 100 μL of saline and (PB+DOX)@(Fe$_3$O$_4$@PEG-PLGA).

were characterized using fluorescent microscopy (CTR 6000, Leica Microsystems Inc., Germany).

2.18. Statistical analysis

Parametric data are presented as the means ± standard deviation (SD). GraphPad Prism version 5.0 (California, USA) was used for the statistical analyses. All statistical comparisons between two groups were performed using the two-sided, nonpaired *t*-test. Differences were considered significant at $p < 0.05$.

3. Result and discussion

3.1. Preparation and characterization of PB@(Fe$_3$O$_4$@PEG-PLGA) MCs

By means of a high-temperature reaction of (Fe(acac)$_3$), 1,2-hexadecanediol, oleic acid and oleylamine, Fe$_3$O$_4$ NPs were feasibly synthesized with a mean diameter of 6 nm and a narrow size distribution (Fig. S1A). Owing to the surface capping agent of citric acid, PB NPs with a mean diameter of 50 nm were also easily obtained from the coprecipitation of FeCl$_3$ and K$_4$[Fe(CN)$_6$] aqueous solutions with good colloidal stability and high hydrophilicity (Fig. S1B). The XRD pattern (Fig. S2A, B) disclosed that all diffraction peaks were well matched with standard powder diffraction data of Fe$_3$O$_4$ NPs and PB NPs in position and relative intensity. In this case, PB@(Fe$_3$O$_4$@PEG-PLGA) MCs were prepared via the PME method, by which hydrophilic PB NPs were encapsulated into

the cavities in the inner water phase and hydrophobic Fe$_3$O$_4$ NPs were loaded in the shell of MCs in the oil phase. The as-prepared PB@(Fe$_3$O$_4$@PEG-PLGA) MCs had a mean diameter of 3.6 μm with a low PDI of 0.04 (Fig. 1A, D) and possessed rough surfaces due to gathering of PEG segments (Fig. 1B). After cutting the MCs by a super thin razor blade, an inner bowl-like hemisphere with a ca. 80-nm-thick shell was clearly observed in Fig. 1C, demonstrating the hollow core/shell structure that was favorable for enhancing the backscattering signal for USI and constructing the high loading efficiency of drug delivery system. On account of the intrinsic magnetic property of embedded Fe$_3$O$_4$, PB@(Fe$_3$O$_4$@PEG-PLGA) MCs could orderly aggregate at the high-field site upon exposure into external magnetic field and quickly disperse in normal saline again once removal of the magnet stimuli (Fig. 1E). No observations of remnant magnetization in hysteresis loops (Fig. 1F) indicated the superparamagnetic characteristic of MCs that was conducive to increasing their local concentration *in vivo*. Combinedly, these results revealed the successful loading of Fe$_3$O$_4$ NPs into the PB@(Fe$_3$O$_4$@PEG-PLGA) MCs. In addition, encapsulation of hydrophilic PB NPs into the MCs was proved by UV–vis spectra, in which the curve of PB NPs extracted from PB@(Fe$_3$O$_4$@PEG-PLGA) MCs was in line with that of pure PB NPs in water (Fig. 1G and H). The tiny difference was attributed to the disturbance of other components in the MCs, but the well-matched maximum absorptions at 697 nm testified the exact encapsulation of PB NPs into the MCs (Fig. 1G, I). The XPS spectra of PB@(Fe$_3$O$_4$@PEG-PLGA) MCs also proved the successful encapsulation of Fe$_3$O$_4$ NPs and PB NPs as observed in Fig. S2C.
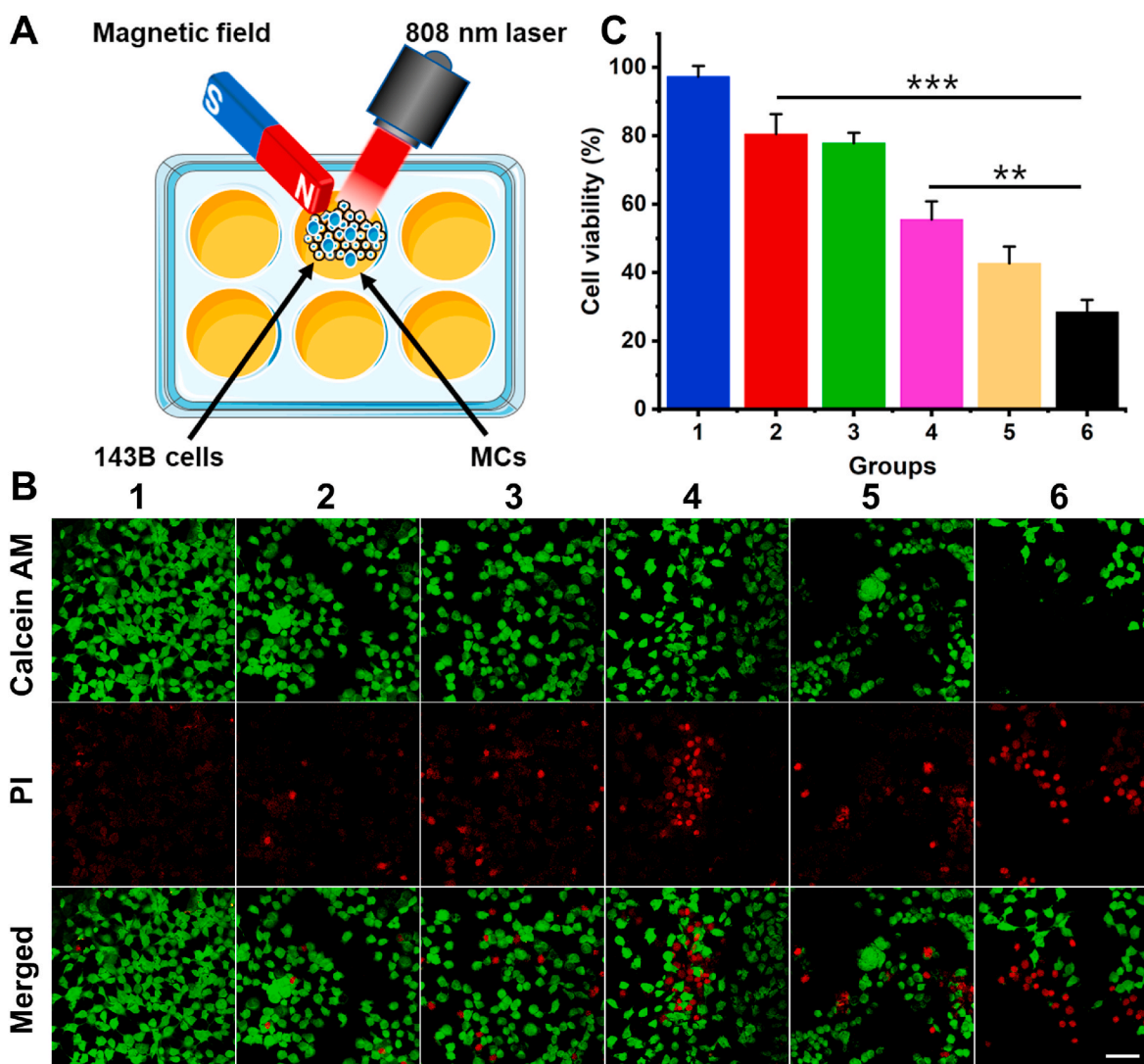
Fig. 4. (A) Schematic illustration of MCs for synergistic therapy *in vitro*. (B) The confocal laser scanning microscopy observation and (C) the viability of 143B cells after treated for 24 h with different groups: (1) Control; (2) PB@(Fe$_3$O$_4$@PEG-PLGA) MCs + NIR laser; (3) (PB+DOX)@(Fe$_3$O$_4$@PEG-PLGA) MCs; (4) (PB+DOX)@ (Fe$_3$O$_4$@PEG-PLGA) MCs + Magnetic field; (5) (PB+DOX)@(Fe$_3$O$_4$@PEG-PLGA) MCs + NIR laser; (6) (PB+DOX)@(Fe$_3$O$_4$@PEG-PLGA) MCs + Magnetic field + NIR laser. Scale bar = 100 μm **$p < 0.01$, ***$p < 0.001$.

Although PLGA and PB biomaterials had been approved by FDA, it was still necessary to assess the biosecurity of PB@(Fe$_3$O$_4$@PEG-PLGA) MCs. NIH/3T3 cells were applied to evaluate the cytotoxicity of MCs via CCK-8 assay. As shown in Fig. S4, no significant difference of cell activity was observed between PB@(Fe$_3$O$_4$@PEG-PLGA) MCs and the control, manifesting that the NIH/3T3 cells could grow well with MCs and evidencing the biocompatibility of PB@(Fe$_3$O$_4$@PEG-PLGA) MCs for the biomedical applications.

3.2. Multi-modality imaging in vitro and in vivo

In views of the distinct structures and advanced properties, these biocompatible PB@(Fe$_3$O$_4$@PEG-PLGA) MCs could function as efficient multi-modality contrast agents to simultaneously enhance US, MR and PAT imaging performance. The US images of MCs dispersed in normal saline were captured under flow state simulating blood circulation to evaluate their contrast effect. As shown in Fig. S5A, compared to the normal saline, Fe$_3$O$_4$@PEG-PLGA and PB@(Fe$_3$O$_4$@PEG-PLGA) MCs showed strong ultrasound signal originating from the great improvement of backscattering signals to US waves. Notably, no significant difference of US signal was observed between Fe$_3$O$_4$@PEG-PLGA and

PB@(Fe$_3$O$_4$@PEG-PLGA) MCs, demonstrating that the encapsulation of PB NPs into Fe$_3$O$_4$@PEG-PLGA MCs did not affect their excellent USI performance (Fig. S5B). After intravenous injection of PB@(Fe$_3$O$_4$@-PEG-PLGA) MCs into the rabbits, Fig. 2A and B exhibited the obvious USI contrast enhancement with more clearly physiological details of heart, which indicated their outstanding USI effect *in vivo*.

Also, we evaluated their MRI contrast enhancement effect via an experimental 7-T MRI instrument. Along with the increase of MCs concentration (1–6 mg/mL), T_2-weighted images became darker in Fig. S6A, manifesting the better contrast for T_2-weighted MRI. Furthermore, the relaxation rate of PB@(Fe$_3$O$_4$@PEG-PLGA) MCs was also depended linearly on their concentration (Fig. S6B). *In vivo* bio-distribution examination was carried out in osteosarcoma-bearing nude mice model. It was found that PB@(Fe$_3$O$_4$@PEG-PLGA) MCs were mainly accumulated in the tumor tissues after post-injection. As shown in Fig. 2C and Fig. S6C, an obvious T_2-weighted contrast enhancement with darker image was observed in osteosarcoma as labelled by red circles, certifying the effective contrast agent of PB@(Fe$_3$O$_4$@PEG-PLGA) MCs for T_2-weighted MRI. Importantly, after applying an external magnetic field on the osteosarcoma for 20 min, T_2-weighted contrast was significantly enhanced due to the gather of superparamagnetic MCs
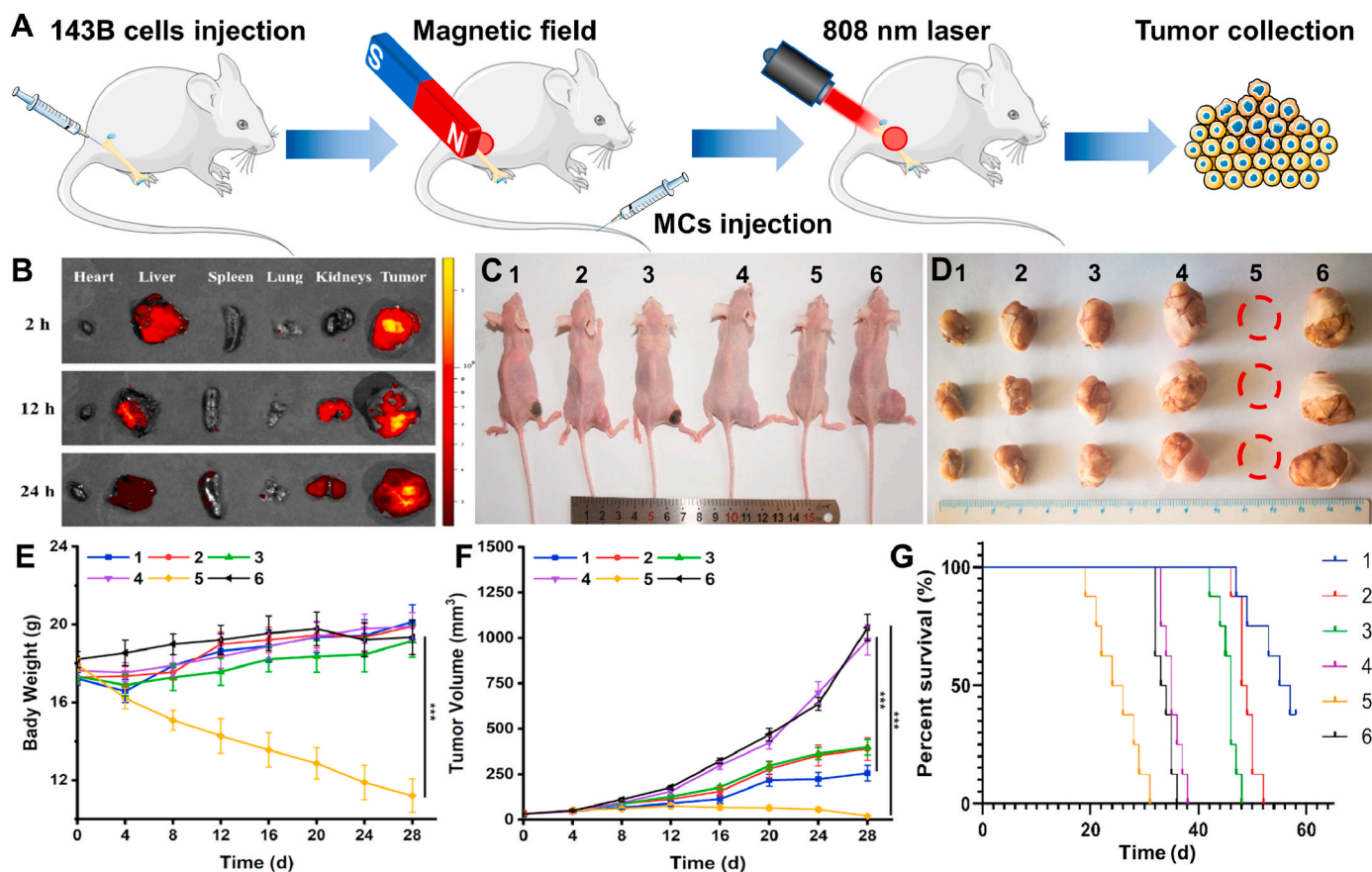
Fig. 5. *In vivo* antitumor effect of osteosarcoma in nude mice. (A) Illustration of photothermal therapy in nude mice. (B) *In vivo* fluorescence imaging and biodistribution of nude mice bearing osteosarcoma at different time points after intravenous injection. (C) Representative images of tumor-bearing nude mice after treated with varied groups under magnetic field: (1) (PB+DOX)@(Fe$_3$O$_4$@PEG-PLGA) MCs + NIR laser; (2) (PB+DOX)@(Fe$_3$O$_4$@PEG-PLGA) MCs; (3) PB@(Fe$_3$O$_4$@PEG-PLGA) MCs + NIR laser; (4) PB@(Fe$_3$O$_4$@PEG-PLGA) MCs; (5) DOX; (6) Saline. (D) Pictures of tumors obtained from nude mice on day 28 after receiving different treatments. Changes of (E) body weights and (F) tumor volumes after treatments for 28 days (n = 6). ***p < 0.001. (G) Survival rate of osteosarcoma tumor-bearing nude mice as a function of time after treatments (n = 8).

under the magnetic field (Fig. 2D). Thus, it was concluded that PB@(Fe$_3$O$_4$@PEG-PLGA) MCs could achieve the magnetic targeted contrast enhancement for T_2-weighted MRI.

On account of the encapsulation of PB NPs within the MCs, PB@(Fe$_3$O$_4$@PEG-PLGA) MCs also possessed outstanding PAT contrast effect. We utilized Au NRs as a control for PAT due to their strong absorbance in the NIR. Similarly, Au NR@(Fe$_3$O$_4$@PEG-PLGA) MCs were prepared via PME method. By means of seed mediated growth approach, Au NRs with a mean length-diameter ratio of 3.2:1 (Fig. S7A) were encapsulated into the MCs by evidence of UV–vis spectra. Likewise, although Au NR@(Fe$_3$O$_4$@PEG-PLGA) MCs and pure Au NRs in water were not fully in line with each other, both of their maximum absorptions were located at 510 and 713 nm, revealing Au NRs were encapsulated into the MCs (Fig. S7B-D). PB@(Fe$_3$O$_4$@PEG-PLGA) and Au NR@(Fe$_3$O$_4$@PEG-PLGA) MCs exhibited the same contrast enhancement for PAT in the beginning. However, contrast effect of Au NR@(Fe$_3$O$_4$@PEG-PLGA) MCs decreased sharply at 2 min and weakened to zero at 6 min (Fig. S8A) while PB@(Fe$_3$O$_4$@PEG-PLGA) MCs could maintain a high level even for 60 min, attesting the outstanding PAT contrast agents of PB@(Fe$_3$O$_4$@PEG-PLGA) MCs. The change of photoacoustic signals provided another evidence in Fig. S8B. We analyzed the UV–vis spectra of these two MCs before and after 1 h of PAT, and found that the absorption spectrum of PB@(Fe$_3$O$_4$@PEG-PLGA) MCs showed no significant change while absorption peak of Au NR@(Fe$_3$O$_4$@PEG-PLGA) MCs completely disappeared, demonstrating the excellent photostability of PB@(Fe$_3$O$_4$@PEG-PLGA) MCs for PAT (Fig. S9C). PAT was performed on the tumor before and after injection of PB@(Fe$_3$O$_4$@PEG-

PLGA) MCs into tumor-bearing nude mice through tail veins. While the intrinsic photoacoustic signals were rather week in the tumor before injection (Fig. 2E), the tumor lightened up after injection of PB@(Fe$_3$O$_4$@PEG-PLGA) MCs owing to the circulation of PB@(Fe$_3$O$_4$@PEG-PLGA) MCs in the blood (Fig. 2F). The photoacoustic signal-to-noise ratio could be improved by PB@(Fe$_3$O$_4$@PEG-PLGA) MCs with high NIR absorbance to minimize the light scattering effect.

3.3. DOX loading and NIR-responsive drug release

Hydrophilic DOX could be encapsulated together with PB NPs into the Fe$_3$O$_4$@PEG-PLGA MCs via PME method to prepare (PB+DOX)@(Fe$_3$O$_4$@PEG-PLGA) MCs for construction of integrated photothermal therapy and NIR-responsive drug delivery. The DOX encapsulation efficiency was tested to be 36.4 ± 4.2%, and the drug release behavior was evaluated upon the magnetic field and NIR laser irradiation. As a control, Fig. 3A showed that 15.5 ± 2% of DOX was sustainedly released from (PB+DOX)@(Fe$_3$O$_4$@PEG-PLGA) MCs during 6 h of incubation. With the implement of magnetic field, the drug release rate reached 19.5 ± 2.5%, which may ascribe to the ordered orientation arrangement of Fe$_3$O$_4$ NPs that significantly reduced the resistance to movement of free DOX. In addition, upon irradiation with NIR laser, the increasing temperature by photothermal PB NPs not only powerfully promoted the DOX movement but also surpassed the glass transition temperature (45–55 °C) of PEG-PLGA (Fig. S3A), thus resulting in the fracture of MCs and subsequent rapid release of the encapsulated drugs (Fig. S3B). It was mentioned that although the PB NPs has a maximum peak absorption at
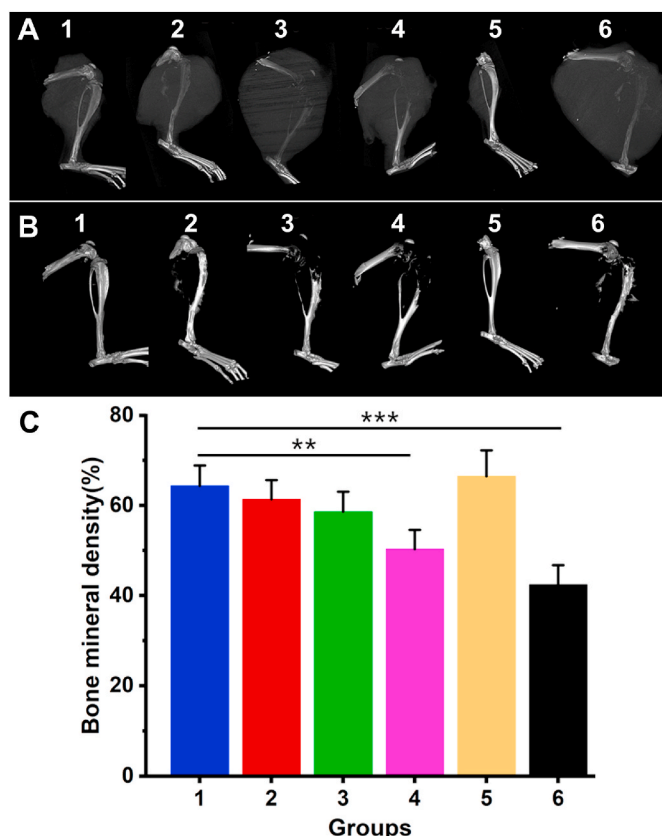
Fig. 6. Micro-CT and BMD of nude mice treated with photothermal therapy. (A) Micro-CT images of the right hind leg of nude mice (with tumor). (B) Micro-CT images of the right hind leg of nude mice (perspective). (C) Measurement of bone mineral density from different groups (n = 6) at 28 days. (1) (PB+DOX)@(Fe$_3$O$_4$@PEG-PLGA) MCs + NIR laser; (2) (PB+DOX)@(Fe$_3$O$_4$@PEG-PLGA) MCs; (3) PB@(Fe$_3$O$_4$@PEG-PLGA) MCs + NIR laser; (4) PB@(Fe$_3$O$_4$@PEG-PLGA) MCs; (5) DOX; (6) Saline. **$p < 0.01$, ***$p < 0.001$.

697 nm, it also had a high absorbance in the NIR region. From this point of view, a highest release rate of $41.9 \pm 2.6\%$ was reasonably reached under simultaneous NIR laser irradiation and magnetic field. It is noteworthy that the delivery systems with dual magnetic- and NIR-triggered drug release behavior provided the chemotherapy drugs with considerably lower side effects by regulation of intracellular drug release [21]. Therefore, these (PB+DOX)@(Fe$_3$O$_4$@PEG-PLGA) MCs could be utilized as the chemo-photothermal agents for tumor treatment.

3.4. In vitro photothermal therapy

In vitro photothermal experiments were firstly conducted by investigating the changes in the temperature of aqueous solution containing (PB+DOX)@(Fe$_3$O$_4$@PEG-PLGA) MCs under irradiation of NIR laser at 808 nm. The temperature of (PB+DOX)@(Fe$_3$O$_4$@PEG-PLGA) MCs dispersions increased from 37 to 47 °C, whereas DOX@(Fe$_3$O$_4$@PEG-PLGA) MCs showed little change of temperature at the same irradiation condition (Fig. 3B). Additionally, (PB+DOX)@(Fe$_3$O$_4$@PEG-PLGA) MCs showed non-significant changes of photothermal performances during 3 cycles of NIR irradiation, indicating their great NIR light-induced thermal ability for PTT applications, which was testified using 143B cells to establish tumor models in Balb/c nude mice. After injection of (PB+DOX)@(Fe$_3$O$_4$@PEG-PLGA) MCs, an external magnetic field was applied on the tumor site for 20 min, and then the tumor sites were irradiated with the 808-nm laser (0.8 W cm^{-2}) for 10 min every 48 h. To monitor the photothermal effects *in vivo*, the infrared thermos graphic

images and temperature changes within tumors were recorded by an infrared thermal imaging camera (Fig. 3C and D). Under NIR laser irradiation, tumor temperature of nude mice treated with saline was only increased by 4.3 °C while that of nude mice injected with (PB+DOX)@(Fe$_3$O$_4$@PEG-PLGA) MCs was increased to 51.7 °C, which was sufficient for the tumor ablation [58].

To reveal the synergistically magnetic-guided location effect and NIR-induced thermal ability, *in vitro* photothermal therapy of (PB+DOX) @(Fe$_3$O$_4$@PEG-PLGA) MCs on 143B cells was studied by investigation of cell apoptosis in Fig. 4A. PI, as a small molecule dye, can stain the dead cells with damaged cell membranes by emitting red fluorescence. Fig. 4B showed the few dead cells in control group, and PB@(Fe$_3$O$_4$-PEG-PLGA) MCs + NIR laser group and (PB+DOX)@(Fe$_3$O$_4$@PEG-PLGA) MCs group showed the unsatisfied antitumor results via the inefficient photothermal therapy and chemotherapy. However, upon the magnetic field, (PB+DOX)@(Fe$_3$O$_4$@PEG-PLGA) MCs group exhibited an improved chemotherapeutic efficacy with the cell survival rate of $55.6 \pm 5.3\%$ because the ordered orientation arrangement of Fe$_3$O$_4$ NPs lowered the moving resistance of DOX and enriched the high concentration of antitumor drugs. It was mentioned that a great number of dead cells appeared in the exposure region when the (PB+DOX)@(Fe$_3$O$_4$-PEG-PLGA) MCs were added with NIR irradiation for 10 min, proving the synergistic PTT effect and NIR-accelerated DOX release to kill tumor cells in a short period (Fig. 4C). Visibly, the most antitumor effect was found on (PB+DOX)@(Fe$_3$O$_4$@PEG-PLGA) MCs + magnetic field + NIR laser group with only $28.5 \pm 3.5\%$ of cell survival rate, revealing the significant importance of magnetic-guided location effect and synergistic chemo-photothermal therapy on the effective tumor inhibition of these (PB+DOX)@(Fe$_3$O$_4$@PEG-PLGA) agents.

3.5. In vivo photothermal therapy

To maximize the treatment effect and minimize the side effects, it is important to examine *in vivo* distribution and tumor accumulation of (PB+DOX)@(Fe$_3$O$_4$@PEG-PLGA) MCs *in vivo* (Fig. 5A). After intravenous injection with MCs solution, a small magnet was attached onto the tumor. Then the tumors-bearing nude mice were sacrificed at certain time points and major organs were harvested and imaged using *in vivo* fluorescence imaging system. As shown in Fig. 5B, (PB+DOX)@(Fe$_3$O$_4$@PEG-PLGA) MCs exhibited a remarkable accumulation in liver via reticuloendothelial systems (RES) absorption and tumor site (strongest fluorescence signal) within the first 2 h in the help of magnetic fields, presenting the significant tumor targeting effect and prolonged blood circulation time. After 24 h post-injection, fluorescence intensity was gradually weakened in liver tumor regions but improved in kidneys, indicating its metabolic pathways through urine.

For more in-depth penetration in tumors, an NIR laser of 808 nm was employed to evaluate the synergetic chemo-photothermal antitumor *in vivo*. The nude mice bearing osteosarcoma tumor were divided into six groups: (1) (PB+DOX)@(Fe$_3$O$_4$@PEG-PLGA) MCs + NIR laser; (2) (PB+DOX)@(Fe$_3$O$_4$@PEG-PLGA) MCs; (3) PB@(Fe$_3$O$_4$@PEG-PLGA) MCs + NIR laser; (4) PB@(Fe$_3$O$_4$@PEG-PLGA) MCs; (5) free DOX; (6) Saline. Under magnetic field, the treated nude mice were injected with a total drug dose of 2.5 mg kg^{-1} followed by an exposure to 808-nm NIR light for 20 min every 4 days. The tumor volume was monitored within four weeks. The saline and PB@(Fe$_3$O$_4$@PEG-PLGA) MCs without irradiation showed a negligible tumor inhibition while (PB+DOX)@(Fe$_3$O$_4$@PEG-PLGA) MCs group without irradiation inhibited a certain antitumor ability due to the chemotherapy effectiveness. In comparison, a significant therapeutic effect was obtained in the cases of PB@(Fe$_3$O$_4$@PEG-PLGA) MCs + NIR laser by PTT therapy. An appearance of charring spot on the tumor site also indicated that Fe$_3$O$_4$ NPs generated photothermal hemorrhage (Fig. 5C). Notably, combination treatment with (PB+DOX)@(Fe$_3$O$_4$@PEG-PLGA) MCs upon NIR irradiation resulted in the most efficient inhibition of osteosarcoma growth (234.6 ± 53.6 mm^3) than any other single chemotherapy or photothermal group
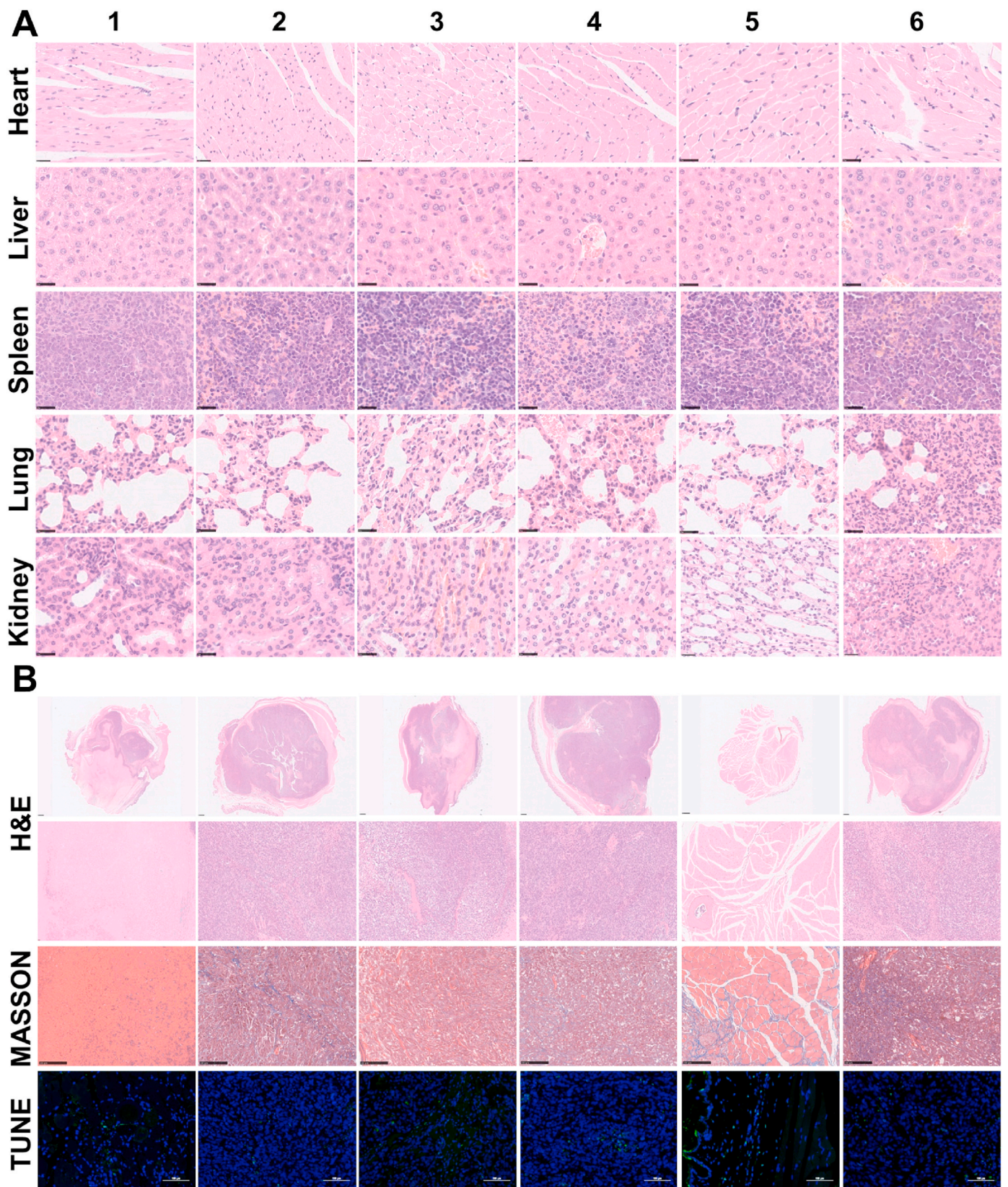
Fig. 7. Histologic assessments of main organs and tumor tissues with and without photothermal treatments. (A) H&E stained images (magnifications are 20 ×) collected from various organs of nude mice in different treatment groups after 28 days: (1) (PB+DOX)@(Fe$_3$O$_4$@PEG-PLGA) MCs + NIR laser; (2) (PB+DOX)@(Fe$_3$O$_4$@PEG-PLGA) MCs; (3) PB@(Fe$_3$O$_4$@PEG-PLGA) MCs + NIR laser; (4) PB@(Fe$_3$O$_4$@PEG-PLGA) MCs; (5) DOX; (6) Saline. (B) H&E, Masson's trichrome and TUNEL staining of tumor slices in different treatment groups after 28 days (magnifications are 1.25 × , 10 × , 10 × and 200 × for columns, respectively).

$(535.7 \pm 69.4 \text{ mm}^3, 636.9 \pm 59.4 \text{ mm}^3, 1289.6 \pm 86.3 \text{ mm}^3$ and $1489.4 \pm 86.4 \text{ mm}^3$), revealing a remarkably enhanced *in vivo* synergistic therapeutic effect (Fig. 5F). Importantly, external magnetic field played significant roles in concentrating these $(PB+DOX)@(Fe_3O_4@PEG-PLGA)$ MCs to tumor site and thus improving the synergistic chemo-photothermal osteosarcoma therapy within the body. The digital photos of nude mice and corresponding excised tumors illuminated that the tumor size treated with $(PB+DOX)@(Fe_3O_4@PEG-PLGA)$ MCs + NIR laser was significantly smaller than other groups (Fig. 5D). Nude mice treated with free DOX showed a gradual decrease in body weight (11.2 $\pm$ 0.8 g), suggesting that DOX had serious side effects, in agreement with previously published literatures [59,60]. As for other treatment groups, the body weight of the nude mice increased to varying degrees (Fig. 5E), indicating the low side effects of these MCs. Nude mice treated with $(PB+DOX)@(Fe_3O_4@PEG-PLGA)$ MCs + NIR laser had a 50% survival rate after 56 days (Fig. 5G). However, all the nude mice treated with free DOX and saline died within 36 days. The other treatments extended lifetimes over the control, but all the nude mice were dead within 52 days. It could be seen that combined chemo-PTT combined treatment can prolong the survival times of nude mice to a much greater extent than single therapy approaches.

Osteosarcoma can cause osteolytic lesions without treatment. To explore the PTT effects on osteosarcoma, the nude mice were killed after 28 days and femoral-scaffold complex samples were immediately collected for micro-CT analysis (Fig. 6A). As shown in the micro-CT images, osteolytic lesions were evident on proximal tibiae in Group 3, 4 and 6 (Fig. 6B and C). Areal bone mineral density of Group 3, 4 and 6 were 58.6 $\pm$ 4.4%, 50.3 $\pm$ 4.2% and 40.2 $\pm$ 4.3%, respectively. In contrast, the areal bone mineral density of $(PB+DOX)@(Fe_3O_4@PEG-PLGA)$ MCs (64.3 $\pm$ 4.6%) remained significantly higher than other groups, which further proved the order of therapeutic effectiveness with synergistic chemo-photothermal therapy > chemotherapy > photothermal therapy. It followed that $(PB+DOX)@(Fe_3O_4@PEG-PLGA)$ MCs with NIR irradiation could significantly inhibit the invasion ability of osteosarcoma and relieves osteolytic lesions.

3.6. Histological analysis

We performed H&E staining of the main organs (heart, liver, spleen, lung and kidney) at 28 days post-injection to evaluate the *in vivo* biosafety after synergistic therapy of $(PB+DOX)@(Fe_3O_4@PEG-PLGA)$ MCs. No evident histopathological lesion was observed in these organs (Fig. 7A), indicating the negligible long-term adverse toxicity towards the major organs. To confirm the efficacy of PTT therapy, H&E, Masson's trichrome and TUNEL staining of tumor slices were performed on day 28 after treatment. As clearly seen in Fig. 7B, H&E staining revealed that there was obviously necrosis region of tumor cells in all the control groups. In striking contrast, tumors treated with $(PB+DOX)@(Fe_3O_4@PEG-PLGA)$ MCs + NIR laser displayed a large number of necrotic cells like DOX group. Masson's trichrome staining showed better-growing muscle fibers in PTT treatment and DOX groups (Groups 1, 3 and 5) than other groups. Likewise, TUNEL staining demonstrated that a large number of apoptotic cells appear in the Groups 1, 3 and 5, while almost no apoptotic cells could be found in other three groups. These stained images of tumor tissues were also captured to confirm the therapeutic effects of different treatments. Apparently, most of tumor cells were destroyed in $(PB+DOX)@(Fe_3O_4@PEG-PLGA)$ MCs group, further confirming that the combined chemo-photothermal therapy could lead to an improved anticancer efficacy, which was accounting for the following reasons: (i) The released DOX could stabilize the topo-isomerase II complex after the DNA chain is broken for replication, and prevent the DNA double helix from resealing, thus stopping the replication process of tumor cells; (ii) PTT could directly kill the tumors via the generated heat and improve cellular uptake by facilitating cell membrane permeability; (iii) PTT could accelerate DOX release to enhance the chemotherapeutic effect; (iv) PTT also had capacities to

modulate the tumor microenvironments by suppressing the macrophages polarization towards the M2 pro-tumor phenotype [61,62].

4. Conclusion

In summary, we have fabricated a new theranostic agent of $(PB+DOX)@(Fe_3O_4@PEG-PLGA)$ MCs with unique US/MR/PAT multi-modality imaging performance and synergistic chemo-photothermal osteosarcoma therapy. Uniform hollow structures and multifunctional payloads benefited these $PB@(Fe_3O_4@PEG-PLGA)$ MCs to achieve excellent properties in biocompatibility, dispersibility, magnetic targeting and photothermal conversion capacities. Under the guidance of magnetic field, $(PB+DOX)@(Fe_3O_4@PEG-PLGA)$ MCs could be accumulated and targeted in the osteosarcoma region, by which local temperature quickly rose up by photochemical transformation to thermally ablate osteosarcoma as well as acceleration of DOX release with NIR irradiation. *In vitro* and *in vivo* results revealed that the combination of chemotherapy and photothermal therapy exerted much higher tumor inhibition efficiency on invasion of osteosarcoma and alleviation of osteolytic lesions, which exceeded the simple superposition of individual therapy methods. Therefore, all these favorable properties confirmed a promising platform of these multifunctional MCs as theranostic agents integrating multiple capabilities, like accurate diagnosis and precise locating of cancerous tissue, as well as effective targeted nanoplatform for tumor therapy.

CRediT authorship contribution statement

Hufei Wang: Conceptualization, Investigation, Methodology, Validation, Writing – original draft. **Sijia Xu:** Conceptualization, Investigation, Methodology, Validation. **Daoyang Fan:** Conceptualization, Investigation, Methodology, Validation. **Xiaowen Geng:** Investigation, Methodology. **Guang Zhi:** Investigation, Methodology. **Decheng Wu:** Investigation, Methodology. **Hong Shen:** Investigation, Methodology. **Fei Yang:** Validation, Conceptualization, Funding acquisition, Supervision, Writing – review & editing. **Xiao Zhou:** Conceptualization, Funding acquisition, Supervision, Writing – review & editing. **Xing Wang:** Conceptualization, Supervision, Writing – review & editing.

Declaration of competing interest

The authors declare no conflict of interest.

Acknowledgment

Appendix A. Supplementary data

Supplementary data to this article can be found online at https://doi.org/10.1016/j.bioactmat.2021.05.004.

References

[1] M. Wilhelm, et al., ENCCAWP17-WP7 consensus paper on teenagers and young adults (TYA) with bone sarcomas, Ann. Oncol. 25 (2014) 1500–1505.
[2] A. Gupte, et al., Systematic screening identifies dual PI3K and mTOR inhibition as a conserved therapeutic vulnerability in osteosarcoma, Clin. Canc. Res. 21 (2015) 3216–3229.
[3] R.H. Blum, Simplified vs complex adjuvant chemotherapy schedule for osteosarcoma, Lancet 350 (1997) 900–901.
[4] R.L. Souhami, et al., Randomised trial of two regimens of chemotherapy in operable osteosarcoma: a study of the european osteosarcoma intergroup, Lancet 350 (1997) 911–917.

[5] M.S. Isakoff, et al., Osteosarcoma: current treatment and a collaborative pathway to success, J. Clin. Oncol. 33 (2015) 3029.

[6] A. Luetke, et al., Osteosarcoma treatment - where do we stand? A state of the art review, Canc. Treat Rev. 40 (2014) 523–532.

[7] P.F. Wei, et al., Vancomycin- and strontium-loaded microspheres with multifunctional activities in antibacteria, angiogenesis and osteogenesis for enhancing infected bone regeneration, ACS Appl. Mater. Interfaces 11 (34) (2019) 30596–30609.

[8] P.M. Anderson, et al., Mifamurtide in metastatic and recurrent osteosarcoma: a patient access study with pharmacokinetic, pharmacodynamic, and safety assessments, Pediatr. Blood Canc. 61 (2014) 238–244.

[9] N. Frazier, et al., Hyperthermia approaches for enhanced delivery of nanomedicines to solid tumors, Biotechnol. Bioeng. 112 (2015) 1967–1983.

[10] N. Datta, et al., Local hyperthermia combined with radiotherapy and-/or chemotherapy: recent advances and promises for the future, Canc. Treat Rev. 41 (2015) 742–753.

[11] H.K. Moon, et al., In vivo near-infrared mediated tumor destruction by photothermal effect of carbon nanotubes, ACS Nano 3 (2009) 3707–3713.

[12] Q. Chen, et al., Recent advances in different modal imaging-guided photothermal therapy, Biomaterials 106 (2016) 144–166.

[13] J.G. Hinman, et al., Layer-by-layer synthesis of conformal metal-organic framework shells on gold nanorods, Chem. Mater. 30 (2018) 7255–7261.

[14] Y. Zhao, et al., Anti-EGFR peptide-conjugated triangular gold nanoplates for computed tomography/photoacoustic imaging-guided photothermal therapy of non-small cell lung cancer, ACS Appl. Mater. Interfaces 10 (2018) 16992–17003.

[15] S. Wu, et al., Silica-coated gold-silver nanocages as photothermal antibacterial agents for combined anti-infective therapy, ACS Appl. Mater. Interfaces 11 (2019) 17177–17183.

[16] H. Shi, et al., Tumor-targeting CuS nanoparticles for multimodal imaging and guided photothermal therapy of lymph node metastasis, Acta Biomater. 72 (2018) 256–265.

[17] C. Hu, et al., Monodispersed CuSe sensitized covalent organic framework photosensitizer with an enhanced photodynamic and photothermal effect for cancer therapy, ACS Appl. Mater. Interfaces 11 (26) (2019) 23072–23082.

[18] J. Wu, et al., Functionalized MoS_2 nanosheet-capped periodic mesoporous organosilicas as a multifunctional platform for synergistic targeted chemo-photothermal therapy, Chem. Eng. J. 342 (2018) 90–102.

[19] A. Tayyebi, et al., Supercritical water in top-down formation of tunable-sized graphene quantum dots applicable in effective photothermal treatments of tissues, Carbon 130 (2018) 267–272.

[20] Y.W. Bao, et al., Platinum-doped carbon nanoparticles inhibit cancer cell migration under mild laser irradiation: multi-organelle-targeted photothermal therapy, Biomaterials 183 (2018) 30–42.

[21] B. Poinard, et al., Polydopamine nanoparticles enhance drug release for combined photodynamic and photothermal therapy, ACS Appl. Mater. Interfaces 10 (2018) 21125–21136.

[22] Q. Zou, et al., One-step synthesis of iodinated polypyrrole nanoparticles for ct imaging guided photothermal therapy of tumors, Small 14 (2018), 1803101.

[23] T. Yang, et al., Ultrastable near-infrared conjugated-polymer nanoparticles for dually photoactive tumor inhibition, Adv. Mater. 29 (31) (2017), 1700487.

[24] G.F. Shu, et al., Sialic acid-engineered mesoporous polydopamine nanoparticles loaded with SPIO and Fe^{3+} as a novel theranostic agent for T1/T2 dual-mode MRI-guided combined chemo-photothermal treatment of hepatic cancer, Bioactive Mater. 6 (5) (2021) 1423–1435.

[25] N.N. Zhang, et al., Gadolinium-loaded calcium phosphate nanoparticles for magnetic resonance imaging of orthotopic hepatocarcinoma and primary hepatocellular carcinoma, Biomater. Sci. 8 (7) (2020) 1961–1972.

[26] J.F. Liao, et al., Gold nanorods and nanohydroxyapatite hybrid hydrogel for preventing bone tumor recurrence via postoperative photothermal therapy and bone regeneration promotion, Bioactive Mater. 6 (8) (2021) 2221–2230.

[27] J. Chen, et al., Doxorubicin-conjugated pH-responsive gold nanorods for combined photothermal therapy and chemotherapy of cancer, Bioactive Mater. 3 (3) (2018) 347–354.

[28] D. Li, et al., Ultrasound-enhanced fluorescence imaging and chemotherapy of multidrug-resistant tumors using multifunctional dendrimer/carbon dot nanohybrids, Bioactive Mater. 6 (3) (2021) 729–739.

[29] Z.J. Fan, et al., Reversing cold tumors to hot: an immunoadjuvant-functionalized metal-organic framework for multimodal imaging-guided synergistic photo-immunotherapy, Bioactive Mater. 6 (2) (2021) 312–325.

[30] L. Cheng, et al., PEGylated prussian blue nanocubes as a theranostic agent for simultaneous cancer imaging and photothermal therapy, Biomaterials 35 (37) (2014) 9844–9852.

[31] C.M. Juliana, et al., CpG-coated prussian blue nanoparticles-based photothermal therapy combined with anti-CTLA-4 immune checkpoint blockade triggers a robust abscopal effect against neuroblastoma, Trans. Oncol. 13 (10) (2020) 100823.

[32] F.F. Chen, et al., Activatable magnetic/photoacoustic nanoplatform for redox-unlocked deep-tissue molecular imaging in vivo via prussian blue nanoprobe, Anal. Chem. 92 (19) (2020) 13452–13461.

[33] Y.J. Liu, et al., Human HSP70 promoter-based prussian blue nanotheranostics for thermo-controlled gene therapy and synergistic photothermal ablation, Adv. Funct. Mater. 28 (32) (2018), 1802026.

[34] M. Zheng, et al., Single-step assembly of DOX/ICG loaded lipid–polymer nanoparticles for highly effective chemo-photothermal combination therapy, ACS Nano 7 (3) (2013) 2056–2067.

[35] K. Pu, et al., Semiconducting polymer nanoparticles as photoacoustic molecular imaging probes in living mice, Nat. Nanotechnol. 9 (3) (2014) 233–239.

[36] L. Cheng, et al., PEGylated Prussian blue nanocubes as a theranostic agent for simultaneous cancer imaging and photothermal therapy, Biomaterials 35 (37) (2014) 9844–9852.

[37] G. Liang, et al., Precise tumor photothermal therapy guided and monitored by magnetic resonance/photoacoustic imaging using a safe and ph-responsive Fe(III) complex, Adv. Healthc. Mater. (2020) 2001300.

[38] Z. Li, et al., Facile layer-by-layer self-assembly toward enantiomeric poly(lactide) stereocomplex coated magnetite nanocarrier for highly tunable drug deliveries, ACS Appl. Mater. Interfaces 8 (3) (2016) 1842–1853.

[39] Y.G. Wang, et al., Enzyme-instructed self-aggregation of Fe_3O_4 nanoparticles for enhanced MRI T-2 imaging and photothermal therapy of tumors, Nanoscale 12 (3) (2020) 1886–1893.

[40] S.J. Xu, et al., Uniform PEGylated PLGA microcapsules with embedded Fe_3O_4 nanoparticles for US/MR dual-modality imaging, ACS Appl. Mater. Interfaces 7 (36) (2015) 20460–20468.

[41] D. Li, et al., Preparation of uniform starch microcapsules by premix membrane emulsion for controlled release of avermectin, Carbohydr. Polym. 136 (2016) 341–349.

[42] B.X. Liu, et al., Fabrication of uniform sized polylactone microcapsules by premix membrane emulsification for ultrasound imaging, Polym. Chem. 5 (5) (2014) 1693–1701.

[43] Z.Y. Yuan, et al., Dual-controlled release of icariin/Mg^{2+} from biodegradable microspheres and their synergistic upregulation effect on bone regeneration, Adv. Healthc. Mater. 9 (11) (2020), 2000211.

[44] Z.Y. Yuan, et al., Injectable PLGA microspheres with tunable magnesium ions release for promoting bone regeneration, Acta Biomater. 85 (2019) 294–309.

[45] Y.P. Li, et al., PEGylated PLGA nanoparticles as protein carriers: synthesis, preparation and biodistribution in rats, J. Contr. Release 71 (2) (2001) 203–211.

[46] K. Xiao, et al., The effect of surface charge on in vivo biodistribution of PEG-oligocholic acid based micellar nanoparticles, Biomaterials 32 (13) (2011) 3435–3446.

[47] Z. Li, et al., Safe and efficient membrane permeabilizing polymers based on PLLA for antibacterial applications, RSC Adv. 6 (34) (2016) 28947–28955.

[48] W. Li, et al., Reduction-responsive shell cross-linked micelles derived from amphiphilic triblock copolymer as anticancer drug delivery carrier, Mater. Sci. Eng. C 96 (2019) 383–390.

[49] T. Niidome, et al., PEG-modified gold nanorods with a stealth character for in vivo applications, J. Contr. Release 114 (3) (2016) 343–347.

[50] Z. Li, et al., Recent advances in stereocomplexation of enantiomeric PLA-based copolymers and applications, Prog. Polym. Sci. 62 (2016) 22–72.

[51] L. Jiang, et al., PHA-based thermogel as a controlled zero-order chemotherapeutic delivery system for the effective treatment of melanoma, ACS Appl. Bio Mater. 2 (2019) 3591–3600.

[52] W. Li, Stereo complexed micelle formation through enantiomeric PLA-based Y-shaped copolymer for targeted drug delivery, Mater. Sci. Eng. C 91 (2018) 688–695.

[53] S.H. Sun, et al., Monodisperse MFe_2O_4 (M = Fe, Co, Mn) nanoparticles, J. Am. Chem. Soc. 126 (1) (2004) 273–279.

[54] M. Shokouhimehr, et al., Biocompatible prussian blue nanoparticles: preparation, stability, cytotoxicity, and potential use as an MRI contrast agent, Inorg. Chem. Commun. 13 (1) (2010) 58–61.

[55] B.Y. Xu, et al., tLyP-1-conjugated Au-nanorod@SiO_2 core-shell nanoparticles for tumor-targeted drug delivery and photothermal therapy, Langmuir 30 (26) (2014) 7789–7797.

[56] D. Huang, et al., Isoniazid conjugated poly(lactide-co-glycolide): long-term controlled drug release and tissue regeneration for bone tuberculosis therapy, Biomaterials 52 (2015) 417–425.

[57] J. Zhang, et al., Ionic colloidal molding as a biomimetic scaffolding strategy for uniform bone tissue regeneration, Adv. Mater. 29 (17) (2017), 1605546.

[58] L. Qiang, et al., A novel macrophage-mediated biomimetic delivery system with NIR-triggered release for prostate cancer therapy, J. Nanobiotechnol. 17 (1) (2019) 83.

[59] E. Li, et al., Multifunctional magnetic mesoporous silica nanoagents for in vivo enzyme-responsive drug delivery and mr imaging, Nanotheranostics 2 (3) (2018) 233–242.

[60] X. Liu, et al., Water-responsive hybrid nanoparticles codelivering ICG and DOX effectively treat breast cancer via hyperthermia-aided DOX functionality and drug penetration, Adv. Healthc. Mater. 8 (8) (2019), 1801486.

[61] X. Deng, et al., Polarization and function of tumor-associated macrophages mediate graphene oxide-induced photothermal cancer therapy, J. Photochem. Photobiol. B Biol. 208 (2020), 111913.

[62] H. Zhu, et al., Doxorubicin redox biology: redox cycling, topoisomerase inhibition, and oxidative stress, React. Oxygen Species (Apex, NC) 1 (3) (2016) 189–198.